A Millimeter-Scale Crystal-Less MICS Transceiver for Insertable Smart Pills

A Millimeter-Scale Crystal-Less MICS Transceiver for Insertable Smart Pills

Minyoung Song, *Member, IEEE*, Ming Ding, *Member, IEEE*, Evgenii Tiurin, Kai Xu, *Student Member, IEEE*, Erwin Allebes, Gaurav Singh, Peng Zhang, Hubregt J. Visser, *Senior Member, IEEE*, Reza Aminzadeh, Wout Joseph, *Senior Member, IEEE*, Luc Martens, *Member, IEEE*, Nick Van Helleputte, *Member, IEEE*, Christian Bachmann, and Yao-Hong Liu, *Senior Member, IEEE*

***Abstract*—This paper presents a millimeter-scale crystal-less wireless transceiver for volume-constrained insertable pills. Operating in the 402–405 MHz medical implant communication service (MICS) band, the phase-tracking receiver-based over-the-air carrier recovery has a $\pm$160 ppm coverage. A fully integrated adaptive antenna impedance matching solution is proposed to calibrate the antenna impedance variation inside the body. A tunable matching network (TMN) with single inductor performs impedance matching for both transmitter (TX) and receiver (RX) and TX/RX mode switching. To dynamically calibrate the antenna impedance variation over different locations and diet conditions, a loop-back power detector using self-mixing is adopted, which expands the power contour up to 4.8 VSWR. The transceiver is implemented in a 40-nm CMOS technology, occupying 2 mm^2 die area. The transceiver chip and a miniature antenna are integrated in a 3.5 $\times$ 15 mm^2 area prototype wireless module. It has a receiver sensitivity of $-$90 dBm at 200 kbps data rate and delivers up to $-$25 dBm EIRP in the wireless measurement with a liquid phantom.**

***Index Terms*—Antenna impedance matching, crystal-less radios, carrier frequency offset (CFO) compensation, gastrointestinal (GI) tract, gastroscopy, implantable radios, ingestible devices, implantable devices, medical implant communication service (MICS), medradio, millimeter-scale radios, phase-tracking receivers.**

I. Introduction

GASTROSCOPY is a common diagnostic method for gastrointestinal (GI) diseases, but it can only be performed in hospitals to provide a "one-time" diagnosis. Existing ingestible pills, e.g., capsule endoscopy [1], can collect patient's GI information over a longer period outside the hospital, and various sensors can be incorporated to collect more information. However, ingestible pills pass through the GI tract along with the food bolus and hence cannot record in specific places of interest over a longer period.

To overcome this issue, one approach is to insert a miniature sensor via the biopsy channel of a gastroscope to a specific area of interest. The device can be attached to the surface wall of the GI tract and record during, for example, a complete digestive cycle after which it detaches itself, and is expelled through natural means [2]. One of the most challenging parts of such "insertable" pill design is the strict volume constraint. Typical biopsy channels in commercial gastroscopes have a diameter of 3.5–4.2 mm (at least 3$\times$ less than existing capsule endoscopy), and the length of the non-bendable part should be shorter than 15 mm. Fig. 1 shows a conceptual scheme of the proposed digestive system and insertable pill. The implant depth (i.e., the distance between the implant and the skin) of the pills typically ranges from 5–15 cm. The implant would interface with an external (wearable) communication hub, with the range between implant and external hub typically $<$2 m.

Wireless communication is a key challenge in such applications. Since the GI is quite deep in the human body, the wireless transceiver should deal with the tissue loss with limited transmission power, to minimize the specific absorption rate (SAR) in human bodies, while fulfilling the strict volume limitation. Moreover, since the power consumption of the wireless transceiver is typically dominant in medical sensor nodes [3], power-efficient transceivers enable a long-term diagnosis with a miniature battery.

In this work, we present a millimeter-scale transceiver for insertable pill applications [4]. The novelties presented in this paper are as follows. First, external crystals are completely avoided by a network-assisted carrier recovery exploiting a phase-tracking receiver. Second, a fully integrated antenna impedance matching solution for covering wide impedance variation of the miniature antenna in the GI tract is realized.

This paper is organized as follows. System-level design considerations for the wireless transceiver will be introduced in Section II. Section III provides design challenges in the miniature insertable transceiver. Section IV describes the circuit

Manuscript received July 30, 2020; revised October 1, 2020; accepted October 26, 2020. Date of publication November 10, 2020; date of current version December 30, 2020. This paper was recommended by Associate Editor Alison J Burdett. *(Corresponding author: Minyoung Song.)*

Minyoung Song, Ming Ding, Evgenii Tiurin, Erwin Allebes, Gaurav Singh, Peng Zhang, Hubregt J. Visser, Christian Bachmann, and Yao-Hong Liu are with the IMEC-Netherlands,, 5656 AE Eindhoven, The Netherlands (e-mail: minyoung.song@imec.nl; ming.ding@imec.nl; erwin.allebes@imec.nl; gaurav.singh@imec.nl; peng.zhang@imec.nl; peng.zhang@imec.nl; christian.bachmann@imec.nl; yao-hong.liu@imec.nl).

Kai Xu is with the IMEC-Netherlands, 5656 AE Eindhoven, The Netherlands. He is now with the equal1.lab/University College Dublin, D14 YH57 Dublin 4, Ireland (e-mail: kai.xu@ucd.ie).

Reza Aminzadeh, Wout Joseph Aminzadeh, and Luc Martens are with the Department of Information Technology, IMEC-Ghent University, B-9052 Gent, Belgium (e-mail: reza.aminzadeh@ugent.be; wout.joseph@ugent.be; luc1.martens@ugent.be).

Nick Van Helleputte is with the IMEC, Leuven 3001, Belgium (e-mail: vhelle@imec.be).

Color versions of one or more of the figures in this article are available online at https://ieeexplore.ieee.org.

Digital Object Identifier 10.1109/TBCAS.2020.3036905

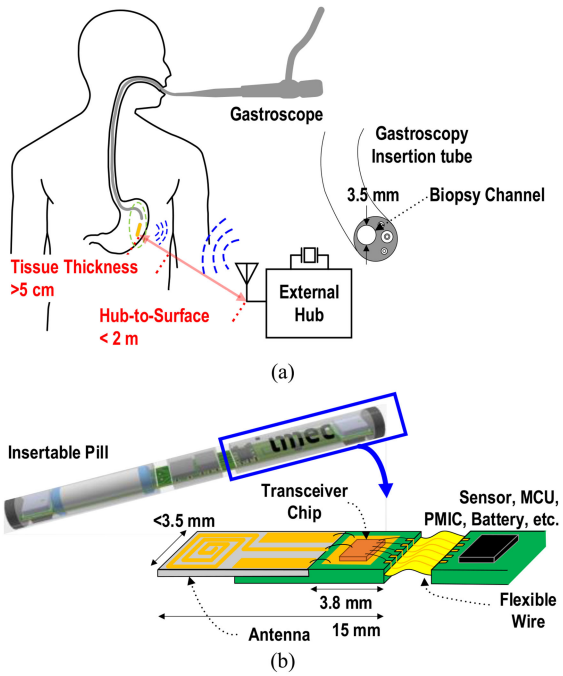

Fig. 1. (a) Conceptual diagram of diagnosing the digestive system with insertable pill and (b) architecture of millimeter-scale wireless node.

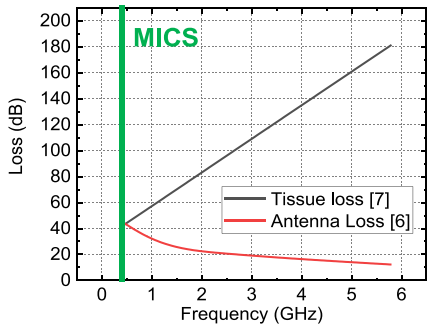

Fig. 2. Frequency dependency on tissue loss (tissue thickness: 7.8 cm) [7], and antenna loss (antenna form factor: 3 x 4 mm^2) [6].

implementations in detail. Section V presents the experimental results. Finally, our conclusions are drawn in Section VI.

II. System Design Considerations

A. Frequency Band Selection

One of the most challenging parts of the radio system in Fig. 1 miniaturization is the antenna size. The antenna efficiency decreases as the antenna size becomes much smaller than the wavelength [5], i.e., the antennas become electrically small. As shown in Fig. 2, higher carrier frequency increases the antenna efficiency with a given dimension [6]. However, the electromagnetic (EM) energy is absorbed more by tissues at higher frequencies [7], and it is even more crucial in deep-implant scenarios, such as ingestible pills.

As illustrated in Fig. 2, assuming that the antenna is a 3×4 mm^2 loop antenna and the tissue thickness is 7.8 cm, it is estimated that the 400 MHz band provides the best link performance. Therefore, the Medical Implant Communication Service (MICS) frequency band (the core band is 402 to 405 MHz) is chosen in this work. Compared to Industrial, Scientific and Medical (ISM) bands e.g., 2.4 GHz or 900 MHz, the MICS band suffers from much less interference and improves power efficiency thanks to a lower carrier frequency. Lower frequency bands such as Near Field Communication (NFC) further reduce the body absorption but are unattractive to ingestible applications due to its short range, limited signal bandwidth and a high sensitivity to misalignments.

TABLE I
Key Regulations of the MICS (Core Band, LBT: Listen Before Talk, LP-LDC: Low-Power, Low-Duty-Cycle)

Parameters			Value
Frequency band			402 – 405 MHz
Maximum channel bandwidth			300 kHz
Temperature range		Implant devices	25 – 45 °C
		Body worn device	0 – 55 °C
Frequency stability			± 100 ppm in temperature range
Transmitter type	LBT	Maximum EIRP	-16 dBm
	LP-LDC	Maximum EIRP	-40 dBm
		Duty cycle	0.01%
		Maximum transmission	10 (during 1-hour interval)

The MICS band is a licensed band for diagnostic and therapeutic medical implants and wearables [8] and targets a communication range of up to 2 meters [9]. One of the key regulations of the MICS band is the frequency accuracy. The frequency stability must maintain ± 100 ppm of accuracy over the applicable temperature range, from 25 °C to 45 °C, for the medical implants. This band also has rules in managing in-band interference for medical use. It limits the maximum equivalent isotropic radiated power (EIRP) to -16 dBm and requires a listen-before-talk (LBT) protocol. Although the LBT protocol mitigates in-band interferences, it requires frequency-agile transceivers that consume significant power because of the frequency monitoring and synchronization of the implant with the external hub. Hence, a low-power, low-duty-cycle (LP-LDC) mode is also defined. With lower maximum EIRP of -40 dBm, limited duty cycle (maximum 0.01% during 1 - hour interval and a maximum 10 transmissions), and a dedicated channel (403.65 MHz), the LP-LDC mode also mitigates the interference without requiring a frequency-agile transceiver [10]. Table I summarizes key regulations of the MICS band.

In this work, we propose an implant-initiation protocol that operates in the LP-LDC mode for initialization, and then later it can support the LBT protocol after initialization, to have a higher flexibility in the wireless link configurations (see Fig. 4).

B. Link Budget Analysis

A link budget analysis is important to understand the impact of the implanted electrically small antenna to the wireless link. To

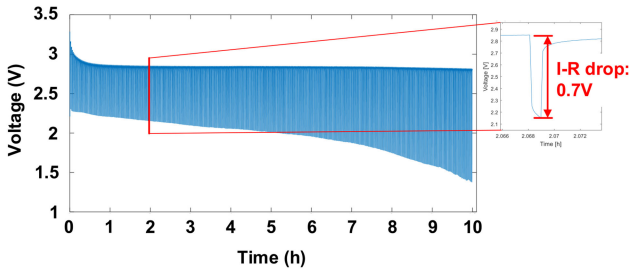

Fig. 3. Measurement result of I-R drop of a millimeter-scale battery (CR-311) with 5 mA pulsed current (pulse width: 3 s and pulse period: 75 s).

meet the millimeter-scale volume constraint, the antenna must be electrically small ($<\lambda/10$), and therefore, the antenna gain of the implant is much smaller than that of the hub. Moreover, EIRP of the implant is even further reduced in the LP-LDC mode. Hence, the uplink and downlink budgets are highly asymmetric.

In the downlink, the received radiated power, P_R can be calculated as

$$P_R = P_{EIRP} - P_{PL} + G_R \tag{1}$$

where P_{EIRP}, P_{PL}, and G_R are the EIRP of the external transmitter through the tissue, the path loss, and the implant receiver antenna gain, respectively. Including fading margin (coverage of 99%), the worst-case P_{PL} measured in a hospital room is ~47 dB [9]. Since the maximum allowable EIRP in the MICS band is −16 dBm, the receiver (RX) sensitivity should be lower than −88 dBm of the maximum P_R, assuming G_R is −25 dBi [4]. The RX sensitivity is defined as

$$S = -174\,\text{dBm/Hz} + 10 \cdot \log(B) + SNR + NF + L \tag{2}$$

where *B, SNR, NF,* and *L* are the bandwidth, the minimum signal to noise ratio, the noise figure, and the implementation loss, respectively. The phase-tracking RX-based FSK demodulation requires *SNR* of 11 dB for bit error rate (BER) of 0.1%, similar to the non-coherent FSK demodulation scheme [11]. Assuming *L* of 10 dB and 300 kHz of *B*, the NF is to be less than 10 dB.

In the uplink, P_R at the hub can be calculated similarly with equation (1). Unlike the downlink, the maximum transmitter EIRP at the implant side is limited to −40 dBm in LP-LDC, so maximum P_R should be lower than −87 dBm, assuming G_R at the hub is 0 dBi.

C. Power Budget Analysis and Duty Cycling

The implantable radio system is typically battery-powered to stay in the body for up to few days. However, small batteries in miniature radios are typically problematic. As the battery size decreases, the battery internal resistance (R_{BAT}), which significantly impacts to the I-R drop, increases. R_{BAT} of millimeter-scale battery increases up to kilo ohms [12]. Therefore, to avoid the battery voltage drop below the core voltage supply and to minimize supply ripples, the active current of the radio should be limited to milli-ampere level. As an example, a millimeter-scale battery (CR-311; 3 × 12 mm^2) has 0.7V I-R drop with 5 mA pulsed current, i. e., R_{BAT} is 140 Ω, as shown in Fig. 3. In this work, the active current during transmission is targeted to be 3–5 mA.

The battery size also limits its capacity. The capacity of millimeter-scale batteries is typically lower than 1 mAh [12]. To sustain the radio operation with an active current of 3 mA and millimeter-scale batteries for up to two days, a duty-cycled operation is mandatory.

Assuming that the system starts up fast and has short post-processing, we can approximate the duty cycle (D) and the average current (I_{AVG}) as

$$D \approx \frac{T_A}{T_A + T_G + T_S} \tag{3}$$

$$I_{AVG} \approx I_s + \frac{I_A \cdot (T_A + T_G)}{T_A + T_G + T_S} \tag{4}$$

where T_A, T_G, T_S, I_A and I_S are active time, guard time, sleep time, active current and sleep current, respectively. The guard time is defined as $T_G = T_S \cdot \epsilon_T$ where ϵ_T is the long-term accuracy of timer. When the battery capacity is 1 mAh, the I_{AVG} should be less than 20.8 μA. In this work, I_S and I_A are 1 μA and 3.1 mA, respectively. Therefore, the duty cycle ratio for up to two days of operation with a 1-mAh battery should be less than 0.64% (assuming ϵ_T is low). To maximize the power efficiency, a stable on-chip 400 kHz real-time clock is adopted as the timer, whose ϵ_T is less than ±20 ppm within the target temperature range (25–45°C) [13]. Such low ϵ_T timer is critical to operate in the ultra-low duty-cycled (i.e., 0.01%) LP-LDC mode.

Assuming that a commercial-of-the-shelf (COTS) millimeter-scale pressure/temperature sensor (TE MS5637-02BA03) is as a GI sensor, the current consumption of the sensor can be excluded from the power budget analysis since it is low (0.6 μA). The sensor data can be collected in a buffer memory and fetched to the radio. When the sensor outputs 24 bits, the total sensor data per hour is 86.4 kb when it senses at every second. When the radio's data rate is 200 kb/s, the required transmission time for the sensor data is 432 ms per hour. The number of transmissions depends on the payload length. With the shortest payload (1 Byte; See Fig. 5(b)), the radio transmits packets 1421 times per hour, i. e., it transmits at every 2.5 seconds.

III. Miniature Transceiver Design

A. Antenna-IC Interface

As described in Section II. B, the electrically small antenna is exploited to meet the millimeter-scale volume constraint. Loop antennas would achieve higher efficiency in conductive body tissues. However, their impedance is too inductive and also too high. Hence, an external matching network, not allowed in the volume constraint, would be additionally required to cover the wide impedance variation in the GI tract. Therefore, in this work, a 3.5 × 10 mm^2 monopole antenna is employed.

Due to its high quality factor, the antenna is sensitive to the environment, e. g., locations, diet conditions, etc. [14]. To evaluate the antenna impedance variation with different diet conditions, a complex body model that comprises different tissue layers was developed in a 3D electromagnetic (EM) simulator

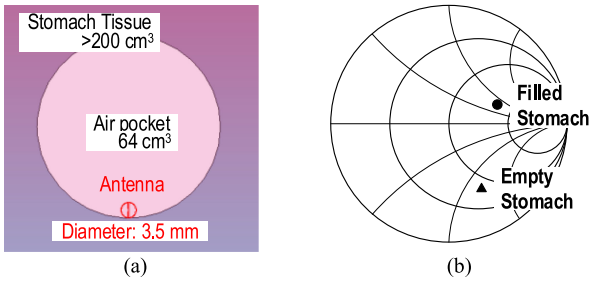

Fig. 4. (a) Diet condition modeling with air pocket. (b) Smith plot of antenna impedance variation with diet condition.

[15]. An air pocket [16] was inserted inside the stomach to emulate the different diet condition in the model as shown in Fig. 4(a). Fig. 4(b) shows the simulation results of the antenna impedance variation with two diet conditions. When the diet condition changes, the antenna impedance can vary up to a factor 4 for the voltage standing wave ratio (VSWR).

Therefore, a tunable matching network (TMN) with matching detection is important to adaptively control the TMN to match to the radio frontend, i.e., power amplifier (PA) and low-noise amplifier (LNA). However, an off-chip TMN requires bulky passive components in the 400 MHz frequency band. Hence, fully integrated antenna impedance matching solutions that minimize the passives [17], [18] are preferable for the TMN design.

The adaptive antenna impedance matching has two detection schemes: direct complex impedance detection and indirect power detection. Direct complex impedance detections [19], [20] are precise, yet their power-hungry hardware with bulky couplers are hardly affordable in the target ingestible applications. Indirect impedance power detections at the antenna are attractive to on-chip integration because of its low power consumption [16], [21]. When a PA has good reverse isolation, the impedance mismatch can be indirectly measured by detecting the amplitude at the antenna.

The impedance detection in the existing solutions needs extra circuits and suffers from a substantial detection time. In this work, we propose an adaptive antenna impedance matching solution with an area-efficient TMN and a loop-back indirect matching detection. Detailed implementation of the antenna impedance matching solution will be described in Section IV.

B. Crystal-Less Transceiver

Another external component limiting the miniaturization is the crystal. Although the crystal is one of the indispensable external components in most of the wireless systems, it is unaffordable in the millimeter-scale insertable device. A film bulk acoustic resonator (FBAR) is an alternative to the quartz crystal in terms of small size [22]. However, it requires a special manufacturing and integration process.

To completely remove the need for crystals or FBARs, network-based synchronizations have been presented [23]–[25]. Two calibration methods are utilized for the network-based synchronization: time calibration [23], [24] and frequency calibration [25].

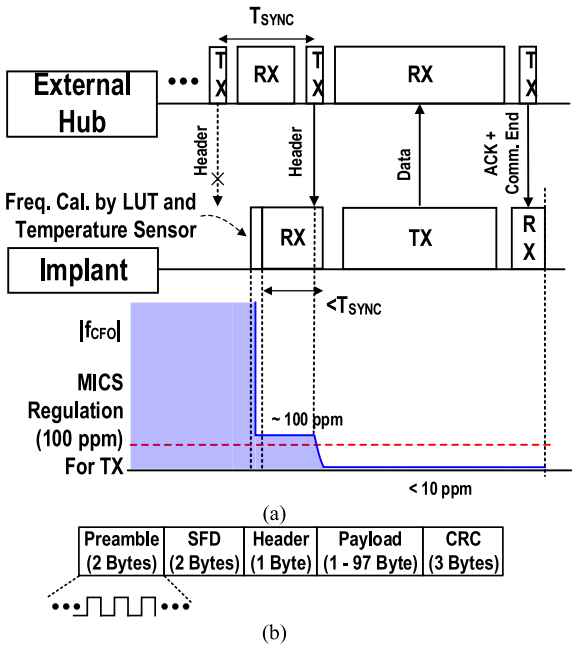

Fig. 5. (a) Proposed implant initiation protocol with carrier synchronization and (b) packet frame.

Protocol-based timing calibrations are typically adopted in noncoherent detection with amplitude or pulse modulations, e.g., on-off-keying (OOK), pulse-position modulation, etc. However, it is unsuitable for the MICS band since the carrier accuracy and stability cannot be guaranteed by the time calibration. Transceivers operating in MICS must achieve a carrier stability better than ± 100 ppm (Table I), which mandates a carrier synchronization for crystal-free operation, and it especially critical for frequency shift keying/ phase shift keying (FSK/PSK) transceivers which are preferred in MICS for their better channel selectivity and adjacent-channel interference resilience. Alternatively, [25] with FSK modulation adopts a frequency calibration to improve the range and accuracy of the carrier synchronization. With an initial temperature calibration by a look-up table (LUT), the transceiver can achieve a stable frequency in a wide temperature range. However, due to the one-time temperature calibration, carrier frequency drift is a potential issue.

Since any transmission from MICS implants must meet the carrier accuracy requirement, this work uses the receiver (RX) assisted by the network to recover the transmitter (TX) carrier before transmission. Unlike a conventional sensor initiating network protocol where the external hub is continuously listening, the proposed MICS-compliant protocol requires the external hub to periodically transmit a header packet, as shown in Fig. 5(a). The temperature dependency of the digitally controlled oscillator (DCO) is first calibrated by a LUT and an on-chip temperature sensor to bring the DCO frequency to within ± 100 ppm. The LUT is configured differently for each transceiver chip so that it reflects the process variation. Then the implant RX is enabled until the header packet is received, and the residue carrier frequency error due to other sources, e.g., supply

variation, LUT error, temperature sensor resolution, etc. are further corrected by the RX (that shares the DCO with the TX) to the same accuracy as the external hub with a crystal (e.g., 10 ppm). During the RX reception, the carrier frequency offset (f_{CFO}) is estimated and compensated during preamble with a repeated 0101 pattern.

To do so, the RX needs to on-the-fly self-calibrate its carrier frequency with the received data. Detailed RX implementation will be introduced in Section IV. Once the DCO frequency is corrected in the RX mode, the implant TX can transmit the sensor data with an accurate carrier, as shown in Fig. 5(a).

A packet frame for the proposed protocol is defined as shown in Fig. 5(b). A 2-byte preamble pattern is used to support the carrier frequency synchronization. a start frame delimiter (SFD) follows for symbol timing synchronization and identification of transmitting node. Payload length can vary from 1 to 97 bytes, followed by a 3-byte cyclic redundancy check (CRC). Error correction coding, e. g. convolution, Reed-Solomon coding with CRC can improve BER/PER and thus the link margin.

The packet length determines the active time (T_A) of the radio. Before the RX activation, the DCO is calibrated in 5 cycles (0.78 µs). Note that the temperature is sensed from the RTC during the sleep time. Before the TX activation, the adaptive matching network (See Section IV. C) is calibrated for 4100 cycles (641 µs). Assuming that the uplink and downlink payload length are both 1 Byte (the shortest), the required duty cycle for the sensor data in Section is approximately (2×9 Bytes $\times 8 \times 200$ kb/s + 0.78 µs + 641 µs) / 2.5 s = 0.05%, which is less than the limit by the battery capacity, 0.64%, but higher than the limit in the LP-LDC mode, 0.01%. Therefore, in the LP-LDC mode, the sensor data throughput, i. e., the frequency of sensing is limited.

IV. Circuit Implementation

A. The Proposed Transceiver Architecture

Fig. 6 shows the block diagram of the proposed MICS transceiver. The Gaussian-FSK (GFSK) TX adopts a direct modulation architecture based on a DCO and a reconfigurable class-D PA. Although the LUT and the RX-assisted carrier recovery correct the carrier frequency before the transmission, such open-loop DCO-based transmitter can have a static frequency shift when the PA is activated, i.e., PA pulling. To minimize this PA pulling, the DCO operates at 1.6 GHz, four times higher than the carrier frequency. By cascading a divider, the reverse isolation can be further enhanced.

The PA output power is programmable, so it not only provides maximum EIRP up to −25 dBm but also supports the LP-LDC transmission with an EIRP below - 40 dBm.

An on-chip 400 kHz real-time clock [13] is utilized to perform duty-cycling with high time accuracy, and it has a built-in temperature sensor with a resolution less than 1 °C. This temperature sensor together with a LUT is used to calibrate the DCO frequency. The RX chain, from LNA to low-pass filter (LPF), is part of two loops: RX-assisted frequency tracking and loop-back antenna matching detection. A single-channel phase-tracking RX uses the same DCO to track the phase of the input signal, while its comparator provides demodulated data

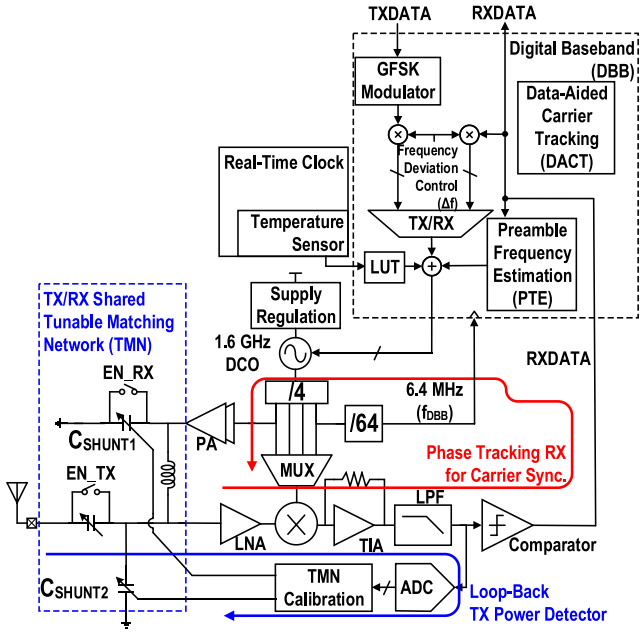

Fig. 6. Block diagram of the proposed MICS transceiver.

[11]. The digital baseband (DBB) clock (f_{DBB}, ∼ 6.3 MHz) is derived directly from the DCO by dividing by 64 in frequency. The maximum symbol rate is 200 kb/s, so the DBB clock has an oversampling ratio of 32 ×. The maximum frequency variation of the DBB clock over the whole band is ∼ ± 0.4% (3MHz/400 MHz), which is negligible to the digital operation, e. g., DCO calibration, phase tracking, TMN. However, it would induce the channel-dependent sampling error on the baseband demodulation when the external hub modulates with the fixed DBB clock (e. g., crystal oscillator). Therefore, The DBB requires a fractional down-sampler, such that channel-dependent sampling frequency has negligible impact in the demodulation.

The RX chain also performs a loop-back TX impedance matching detector. The on-chip TX/RX-shared TMN is calibrated adaptively, depending on the detected mismatch.

B. Phase-Tracking Receiver

The proposed crystal-less transceiver as introduced in Section III. B requires a RX that can adjust its center frequency to the received signal during the reception. Frequency-discrimination RXs [25], [26] extract the frequency from the received signal for the carrier synchronization. The frequency-discrimination technique takes a longer time to extract the frequency to a required precision. Therefore, it is not suitable in insertable pill applications that require agile RX/TX switching and small area.

A phase-tracking RX [11] is employed in this work, as depicted in Fig. 6. Unlike the frequency-discrimination ones, the phase-tracking RX directly locks the phase between its carrier and the received signal. Thanks to its phase-locking behavior, it can realize a single-channel zero-IF RX while avoiding self-corruption [11]. It requires no additional phase detector since the mixer performs as the phase detector as well as the frequency down-converter.

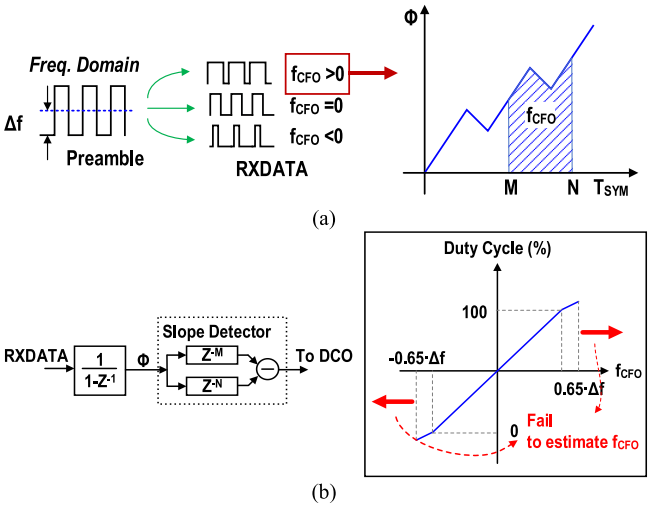

Fig. 7. (a) f_{CFO} dependency on duty cycle of RXDATA and (b) block diagram of proposed PFE and its f_{CFO} coverage.

The mixer-based phase detector gain is input amplitude dependent, defined as $\frac{A_{RF} \cdot A_{LO}}{2} \cdot K_{MX}$, where A_{RF}, A_{LO} and K_{MX} are the amplitude of the mixer inputs and the conversion gain of mixer, respectively. The LPF also serves as a loop filter, whose gain is K_{LPF}. After slicing the LPF output, the comparator modulates the DCO to lock the phase difference to $\frac{\pi}{2}$. The closed-loop transfer function of the phase-tracking RX can be defined as

$$H\ (s) = \frac{\Phi_{LO}\,(s)}{\Phi_{RF}\,(s)} = \frac{\frac{A_{RF} \cdot A_{LO}}{2} \cdot K_{MX} \cdot K_{LPF} \cdot K_{DCO}}{s + \frac{A_{RF} \cdot A_{LO}}{2} \cdot K_{MX} \cdot K_{LPF} \cdot K_{DCO}} \tag{5}$$

where Φ_{LO}, Φ_{RF}, and K_{DCO} are the phase of the mixer inputs and the DCO gain, respectively. With the phase-tracking loop, the DCO frequency is synchronized with the input signal with the phase difference of $\frac{\pi}{2}$ and the comparator outputs the demodulated data (RXDATA). Note that the phase-tracking RX behaves like a type-I phase-locked loop (PLL) since there is no extra pole at origin for the frequency accumulation other than that provided by the DCO. Therefore, the precise DCO frequency setting is an essential prerequisite.

The DCO frequency is first established by the LUT according to the on-chip temperature sensor to within $\pm$100 ppm frequency precision. The initial frequency error is thus within the recovery range of the phase-tracking RX. The carrier recovery of the phase-tracking RX contains two parts: a preamble frequency estimation (PFE) and a data-aided carrier frequency tracking loop (DACT) [11] that continuously tracks the carrier frequency offset.

The PFE is proposed to calibrate the residue carrier frequency error before the DACT, as shown in Fig. 7. By accumulating the demodulated RX output (RXDATA) and detecting the slope at different symbol times (T_{SYM}), the PFE estimate the carrier frequency offset (f_{CFO}). Since f_{CFO} modulates the "duty cycle" of RXDATA during the preamble, the slope of the accumulated

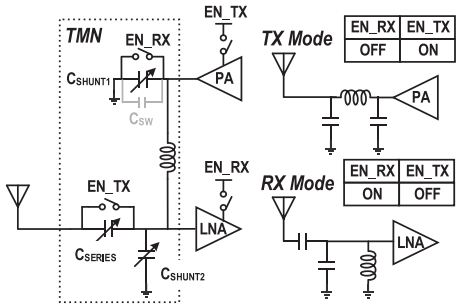

Fig. 8. Proposed single inductor-based TX/RX shared TMN.

RXDATA is used to estimate f_{CFO} as

$$\left(\frac{f_{CFO}}{\Delta f} + 0.5\right) \cdot 100 \;=\; Duty\ Cycle\ of\ RXDATA\,(\%) \tag{6}$$

The f_{CFO} coverage of the phase-tracking RX is determined by the frequency deviation ($\pm\ \Delta f$). In this work, Δf of 100 kHz is chosen based on a trade-off between the RX f_{CFO} coverage and the TX spectrum mask. The DACT then follows to ensure the carrier stability for the rest of the packet. Like the PFE, the DACT also accumulates the RXDATA for frequency tracking but has to refer to a reference phase position, which is given by a proper frequency initialization, e. g., PFE since the RXDATA is random [11].

C. Adaptive Matching Network

To minimize the loss and die area, the TX/RX shared TMN topology using only one inductor is proposed, as shown in Fig. 8. Compared to conventional shared TX/RX matching networks [17], [18], the proposed matching network further reduces loss and area due to multiple inductors. The TMN operates in either TX or RX mode with its mode switches (EN_RX and EN_TX). In RX mode, since the quality factor of the inductor branch is reduced by the on-resistance of the switch EN_RX, EN_RX is sized to minimize the loss and prevent the reduction of the impedance coverage. In addition, EN_RX also works as a fringe capacitor (C_{SW}) in TX mode, which constitutes part of the π-matching network and saves an additional capacitor. The tunability of the proposed TMN is provided by capacitor banks (C_{SERIES}, C_{SHUNT1}, C_{SHUNT2}).

The indirect impedance matching detection typically exploits a power detector at the antenna [16], [21]. However, it consumes additional power and area, and unwanted out-of-band signals along with the TX output power are unavoidable, resulting in unreliable results. The proposed RX-reused matching detection minimizes the hardware overhead and the sensitivity to interference. As illustrated in Fig. 9, the RX chain and an ADC are used as the loop-back power detector that leverages the "self-mixing" principle. Since the input impedance of the inverter based LNA is high, it does not influence the PA impedance matching. The class-D PA structure with cascaded input buffer and divider stages achieves high reverse isolation, so the amplitude at the

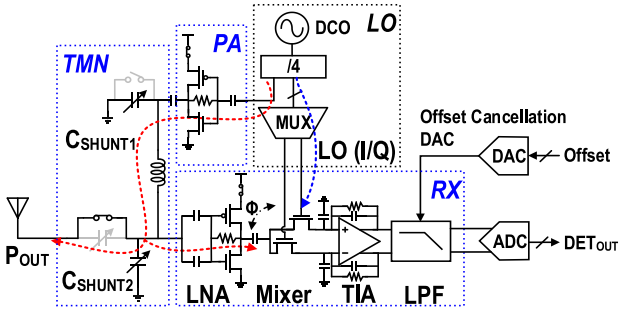

Fig. 9. Proposed loop-back power detection for impedance detection.

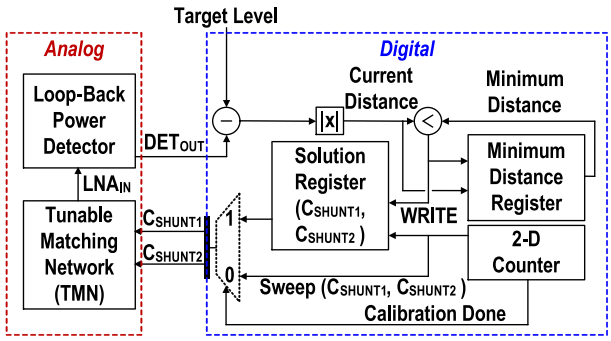

Fig. 10. Block diagram of adaptive TMN calibration.

antenna node (A_{POUT}) primarily depends on the degree of impedance mismatch (i.e., VSWR).

The intrinsic DC offset from transimpedance amplifier (TIA) and low-pass filter (LPF) is first trimmed out by an offset cancellation DAC with TX disabled. Then after the TX is activated, the ADC will produce a DC value (DET_{OUT}) according to the self-mixing of TX and LO signals, which is proportional to A_{POUT}. Since the delay of PA, TMN and LNA introduces a phase difference (Φ) between the mixer's LO and RF ports, A_{POUT} is measured twice with two LO phases, LO (I) and LO (Q), by using a MUX to switch between them, to detect Φ with the single-channel RX. DET_{OUT} with different LO phases can be calculated as

$$\begin{cases} DET_{OUT}\ (I) = A_{POUT}\ \cdot 0.5 \cdot G_{RX} \cdot A_{LO} \cdot \cos(\Phi) \\ DET_{OUT}\ (Q) = A_{POUT}\ \cdot 0.5 \cdot G_{RX} \cdot A_{LO} \cdot \sin(\Phi) \end{cases} \tag{7}$$

where G_{RX} and A_{LO} are RX conversion gain and amplitude of LO output, respectively. Hence, the TX output power (P_{OUT}) can be measured without being affected by Φ as

$$P_{OUT} \propto DE\,T_{OUT} = \sqrt{\left(DET_{OUT}(I)^2 + DET_{OUT}(Q)^2\right)} = A_{POUT} \cdot 0.5 \cdot G_{RX} \cdot A_{LO} \tag{8}$$

A block diagram of the proposed adaptive matching calibration is shown in Fig. 10. During the TMN calibration, two capacitor banks (C_{SHUNT1} and C_{SHUNT2}) are swept until DET_{OUT} exceeds the targeted level. When DET_{OUT} cannot reach the targeted level, the capacitor banks are set where DET_{OUT} is maximum, i.e., P_{OUT} is maximum. This calibration can improve the uplink margin by up to 5 dB. Note that the downlink margin can be compensated by external hub's output power, so the TMN is optimized mainly for the implant TX.

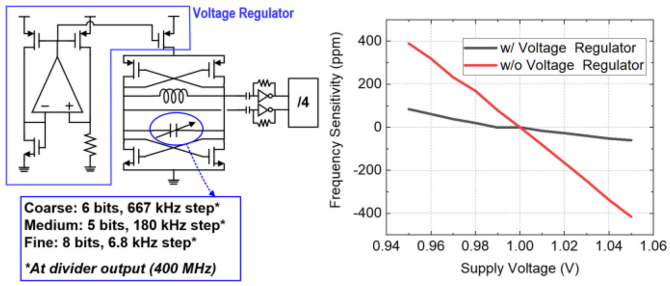

Fig. 11. Simplified diagram of DCO and simulation results of supply sensitivity with and without voltage regulator.

D. Digitally Controlled Oscillator (DCO)

In CMOS technology, a higher frequency oscillator with a frequency divider can reduce power and area of the LC oscillator. Moreover, it can minimize the injection/pulling issue in the zero-IF RX. However, the frequency divider burns extra power. In this frequency band, a quadruple frequency oscillator scheme, as shown in Fig. 11, optimizes power and area consumption. The DCO consists of a complementary cross-coupled pair, an LC tank with three switched capacitor banks, and a voltage regulator. The coarse capacitor bank is to cover process, voltage and temperature (PVT) variations, and the medium bank is to select the frequency channel. The fine bank is used for the direct frequency modulation. The modulation quality is affected by the frequency resolution (Δf_{RES}) in the fine bank and the intrinsic DCO phase noise.

In this work, we target the total frequency modulation error to be less than 10% of frequency deviation not to degrade signal-to-noise ratio (SNR) performance and define Δf_{RES} and the DCO phase noise level, accordingly.

Unlike PLL-based transceivers [22], [27], the open-loop DCO-based transceiver is vulnerable to the long-term frequency drift due to the temperature and supply variation, especially in TX mode. Since the temperature variation is initially calibrated by LUT and the temperature sensor and is negligible during the packet transmission (0.4–4.2 ms), the supply variation is a dominant factor of the frequency drift.

To achieve a high supply regulation to the DCO core, a constant-transconductance (g_m) biased voltage regulator is exploited. Thanks to the voltage regulator, the supply sensitivity is improved by 14.9 dB (see Fig. 11).

V. Measurement Results

The proposed transceiver is implemented in a 40-nm CMOS and occupies 2 mm^2 die area, as shown in Fig. 12(a). The wireless module has an area of 3.5 $\times$ 15 mm^2, including a 3.5 $\times$ 3.8 mm^2 FR-4 printed circuit board (PCB) and a 3.5 $\times$ 10 mm^2 miniature antenna on a high-k ($\varepsilon = 10.7$) Rogers 6010LM substrate. As shown in Fig. 13 (without epoxy), the

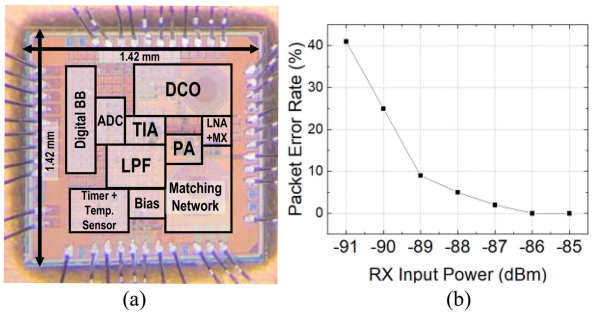

Fig. 12. (a) Die micrograph and (b) Measured RX sensitivity based on PER.

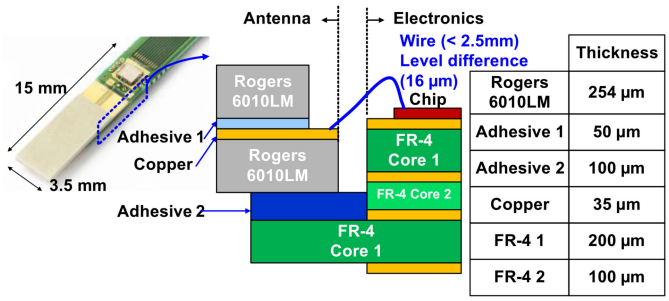

Fig. 13. Integrated wireless module and its vertical view.

TABLE II
PERFORMANCE SUMMARY AND COMPARISON WITH THE STATE-OF-THE-ART MICS AND MM-SCALE TRANSCEIVERS

	This Work	[29] Bachmann VLSI 2015	[30] Lee JSSC 2019	[31] Bae VLSI 2009	[24] Chuo ISSCC 2017	[23] Shi ISSCC 2016	[32] Zhao JSSC 2020
Process (nm)	40	40	180	180	180	180	65
Frequency (MHz)	400	315/400/433	400	400	915	50 (RX) / 112 (TX)	5800
MICS Compliance	Yes				No		
Crystal-less	Yes	No	No	Yes	Yes	Yes	Yes
Supply (TX/RX) (V)	1	1	1.8	0.7	4/1.2	4/1.2	0.8
Modulation (TX/RX)	GFSK	MSK, PSK	OOK	FSK	PPM	PPM/OOK	ASK
RX Sensitivity (dBm)	-90*	-92	-79	-69	-93	-54	N/A
RX DC Power (uW)	1500	2800	92	490	1850	36	N/A
TX Power (dBm)	-6	-16	-4	-6	N/A	N/A	N/A
TX DC Power (mW)	3.1	3	2.8	0.8	2	N/A	N/A
TX Efficiency (%)	8.10%	0.84%	14.22%	31.40%	N/A	N/A	N/A
TX Data Rate (kb/s)	200	455	0.1	250	30.3	2	4.2
On-Chip Tunable Matching Network	Yes	No	No	No	No	No	No
Matching Coverage	4.8 VSWR	N/A	N/A	N/A	N/A	N/A	N/A
Die Area (mm^2)	2	7.3	5.8	N/A**	2.8	2.2	0.08 x 0.08
Electronics Area (mm^2)	3.5 x 3.8	N/A	36 x 35	20 x 20	3 x 3	N/A	0.12 x 0.12
System Volume (mm^2/mm^3)	3.5 x 15	N/A	36 x 54	20 x 20	3 x 3 x 3	1x10	0.12 x 0.12

antenna is stacked on the top of the FR-4 PCB. Layer thickness is carefully considered to minimize the level difference between the antenna and FR-4 board, such that the wire-bonding length can be minimized. The achieved level difference is 16 µm. Table II summarizes the measurement results of the proposed system and compares various parameters with current state of the art.

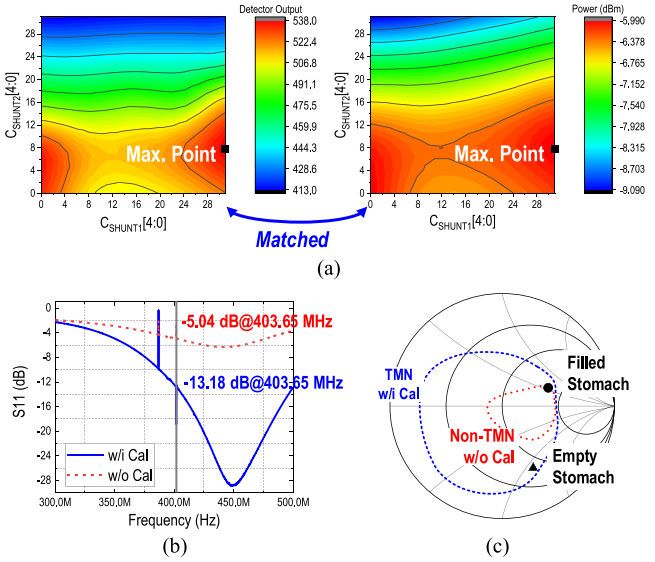

Fig. 14. Measured results at empty stomach condition: (a) TX power detector output and TX output power with sweeping capacitor banks and (b) S_{11}. (c) Measured power contour.

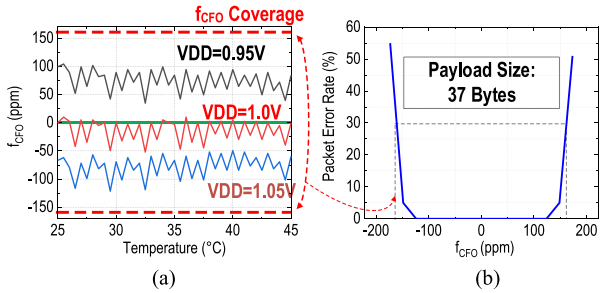

Fig. 15. (a) Measured frequency calibration results by LUT and (b) RX frequency lock-in range ($P_{IN} = -76$ dBm) to achieve less than 30% of PER.

A. Electrical Performance

Fig. 14 shows the measurement result of the proposed loop-back power detector in an empty-stomach condition. The loop-back power detector output matches well with TX output power for different capacitor bank values. The TMN calibration expands the -6-dBm power contour to 4.8 VSWR, which can cover two simulated impedances equivalent to a filled and empty stomach and has an 8-dB improvement of the reflection coefficient (S_{11}) in the empty stomach case.

Fig. 15(a) shows that the LUT-based calibration has ± 125 ppm f_{CFO} when considering $\pm 5\%$ of supply variation, which can be safely recovered by the proposed PT-RX-based carrier synchronization with a measured lock-in range of ± 160 ppm. Thanks to the voltage regulator, the supply sensitivity of the DCO is ± 75 ppm with a 5% supply variation, within the MICS regulation of ± 100 ppm. As shown in Fig. 15(b), the

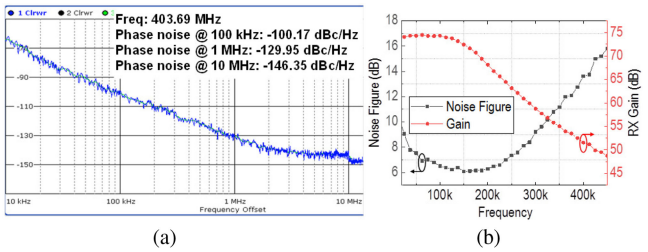

(a) (b)

Fig. 16. Measured (a) DCO phase noise. (b) RX gain and noise figure.

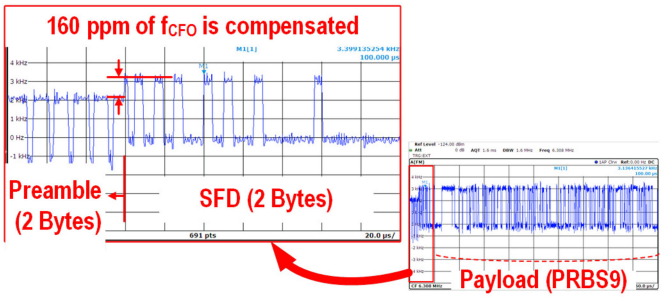

Fig. 17. Transient results of DBB clock (*fDBB*).

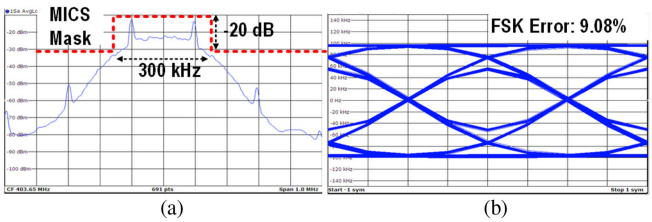

(a) (b)

Fig. 18. (a) TX spectra and (b) eye diagrams 100 kHz Δf.

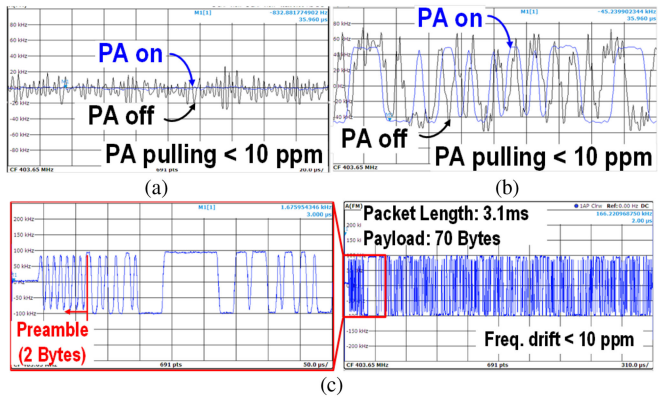

(a) (b) (c)

Fig. 19. (a) PA pulling at (a) continuous wave and (b) GFSK modulation (50 kHz Δf). (c) Frequency drift.

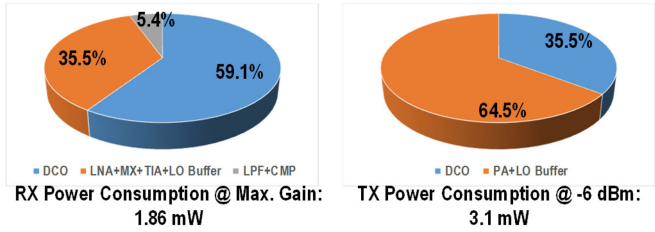

Fig. 20. Power breakdown.

frequency lock-in range of the proposed RX is measured with input power of −76 dBm and the payload size of 37 Bytes.

The measured divided-by-4 DCO phase noise is shown in Fig. 16 (a). The residue FM, integrated from 238 Hz (maximum packet length) to 300 kHz (maximum channel bandwidth), is 2.54 kHz, which is sufficiently below 10% of frequency deviation (10 kHz).

To evaluate the proposed PFE performance, the frequency-domain transient of f_{DBB} ($= f_{DCO}/64$) is measured during packet reception as shown in Fig. 17, f_{CFO} is initially set to 160 ppm, and thus the shown duty cycle of the preamble symbol is higher than 50%. After the PFE, the duty cycle is corrected to 50%, i.e., f_{CFO} is corrected.

The measured RX sensitivity at 200 kb/s is –90.3 dBm with 30% packet error rate (PER), as shown in Fig. 12(b). The measured integrated (up to 300 kHz) noise figure at the maximum gain (74 dB) is 6.1 dB as illustrated in Fig. 16(b).

The transmitter spectra at Δf (100 kHz) satisfy the Federal Communications Commission (FCC) regulation mask [8] as demonstrated in Fig. 18. With pseudo random binary sequence (PRBS) pattern, the TX achieves an FSK error of 9.08 % at Δf of 100 kHz.

As shown in Fig. 19. the measured PA pulling and long-term frequency drift are negligible, indicating that the 4× frequency planning and the good phase noise performance of the DCO demonstrates an excellent TX carrier stability.

Fig. 20 shows the power breakdown of the transceiver. The active current is below 3.1 mA in both TX and RX mode.

B. Wireless Link Setup and Results

Fig. 21(a) shows the wireless measurement setup. The wireless module is placed inside a homogeneous liquid phantom to emulate GI tissues. The module with phantom is placed in front of an SRM field strength analyzer (Narda SRM-3006) at the position of 3 and 5 m away and is rotated over 360 degrees. The phantom consists of de-ionized water, sugar, salt (NaCl), and gelatin [28]. The phantom container is a hemispherical shape with a diameter of 10 cm. With the adaptive impedance matching calibration, the uplink margin is improved by 5 dB, as shown in Fig. 21(b). The EIRP was measured in an outdoor area without objects to minimize the reflections from the environment. Fig. 21(c) shows the measured EIRP at different distances. The similarity of EIRP measured at different distances shows that the reflections from the surrounding environment (mainly ground in this case) are negligible. The measured EIRP at 3 m distance is in the range of −20.6 to −28.9 dBm and averages −25 dBm.

Table II summarizes the performance and benchmarks with state-of-the-art MICS and millimeter-scale transceivers. The presented MICS compatible RX transceiver achieves the smallest volume and has the on-chip antenna impedance matching solution in comparison to other transceivers.

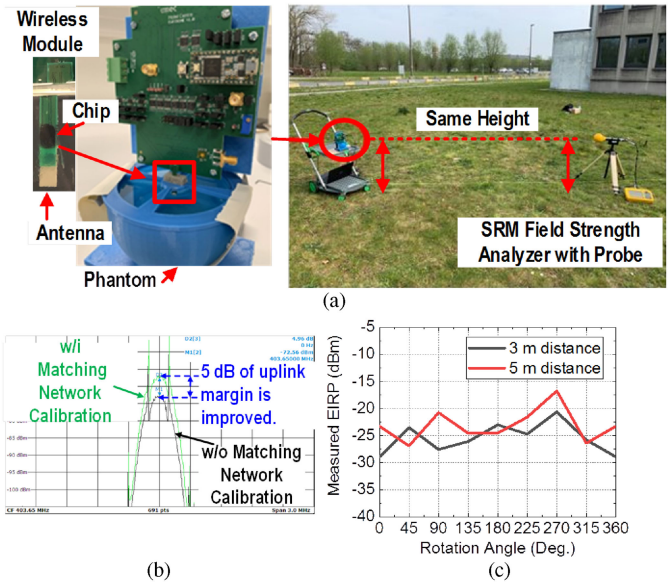

Fig. 21. (a) Wireless measurement setup. (b) Measured wireless TX power improvement by matching network calibration. (c) Measured EIRPs at different distance.

VI. Conclusion

This paper presented a millimeter-scale MICS compatible transceiver to address challenges in insertable/implantable smart pill applications, especially focusing on the high EM absorption in the body and the volume constraint. The MICS band was selected to achieve the optimum link performance with the electrically small antenna and the tissue loss. The link budget and power budget with duty cycling were analyzed to define the design specification. The proposed adaptive antenna impedance matching solution allows wide antenna impedance coverage (4.8 VSWR) without external components. The crystal-less transceiver architecture achieves over-the-air carrier synchronization without crystal by the proposed implant initiation protocol and the phase-tracking RX with a wide carrier frequency lock-in range ($\pm$160 ppm). Implemented in 40-nm CMOS with a 1-V supply, this work achieved a system volume of 3.5 $\times$ 15 mm^2, including the antenna. This is a 30$\times$ smaller system volume than state-of-the-art radios in MICS frequency band, which makes it uniquely suited for extremely volume-constrained medical implants.

References

[1] G. Ciuti, A. Menciassi, and P. Dario, "Capsule endoscopy: From current achievements to open challenges," *IEEE Rev. Biomed. Eng.*, vol. 4, pp. 59–72, 2011.

[2] J. H. Chang *et al.*, "A novel placement method of the bravo wireless pH monitoring capsule for measuring intragastric pH," *Dig. Dis. Sci.*, vol. 54, no. 3, pp. 578–585, Mar. 2009.

[3] A. Ba *et. al.*, "A 0.33 nJ/bit IEEE802.15.6/proprietary MICS/ISM wireless transceiver with scalable data rate for medical implantable applications," *IEEE J. Biomed. Health Informat.*, vol. 19, no. 3, pp. 920–929, May 2015.

[4] M. Song *et. al.*, "A 3.5 mm $\times$ 3.8 mm crystal-less MICS transceiver featuring coverages of $\pm$160 ppm carrier frequency offset and 4.8-VSWR antenna impedance for insertable smart pills," in *Proc. IEEE Int. Solid-State Circuits Conf. (ISSCC) Dig. Tech. Papers*, Feb. 2020, pp. 474–475.

[5] S. Bakogianni and S. Koulouridis, "On the design of miniature medradio implantable antennas," *IEEE Trans. Antennas Propag.*, vol. 65, no. 7, pp. 3447–3445, Jul. 2017.

[6] P. P. Mercier, S. Bandyopadhyay, A. C. Lysaght, K. M. Stankovic, and A. P. Chandrakasan, "A Sub-nW 2.4 GHz transmitter for low data-rate sensing applications," *IEEE J. Solid-State Circuits*, vol. 49, no. 7, pp. 1463–1474, Jul. 2014.

[7] Y. Liu and R. D. Gitlin, "A phenomenological path loss model of the in vivo wireless channel," in *Proc. IEEE Wireless Microw. Tech. Conf.*, Apr. 2015, pp. 1–3.

[8] in *FCC 47 CFR Part 95, Subpart 1, Medical Device Radio Communications Service, FCC*, WA, DC, 2020.

[9] A. H. Johansson, "Performance of a radio link between a base station and a medical implant utilizing the MICS standard," in *Proc. IEEE Int. Conf. Eng. Med. Bio. Soc. (IEMBS)*, Sep. 2004, pp. 2113–2116.

[10] B. Sutton, P. Stadnik, J. Nelson, and L. Stotts, "Probability of interference between LP-LDC and LBT MICS implants in a medical care facility," in *Proc. IEEE Int. Conf. Eng. Med. Bio. Soc. (IEMBS)*, Aug. 2007, pp. 6721–6725.

[11] Y.-H. Liu, V. K. Purushothaman, C. Bachmann, and R. B. Staszewski, "Design and analysis of a DCO-based phase-tracking RF receiver for IoT applications," *IEEE J. Solid-State Circuits*, vol. 54, no. 3, pp. 785–795, Mar. 2019.

[12] I. Lee, Y. Lee, D. Sylvester, and D. Blaauw, "Battery voltage supervisors for miniature IoT systems," *IEEE J. Solid-State Circuits*, vol. 51, no. 11, pp. 2743–2756, Jul. 2016.

[13] M. Ding, M. Song, E. Tiurin, S. Traferro, Y.-H. Liu, and C. Bachmann, "A 0.9pJ/cycle 8ppm/oC DFLL-based wakeup timer enabled by a deterministic time-domain trimming and an embedded temperature sensing," in *Proc. Symp. VLSI Circuits*, Jun. 2020, pp. 1–2.

[14] H.-Y. Lin, M. Takahashi, K. Saito, and K. Ito, "Characteristics of electric field and radiation pattern on different locations of the human body for in-body wireless communication," *IEEE Trans. Antennas Propag.*, vol. 61, no. 10, pp. 5350–5354, Oct. 2013.

[15] J. Kim and Y. Rahmat-Samii, "Implanted antennas inside a human body: Simulations, designs and characterizations," *IEEE Trans. Microw. Theory Techn.*, vol. 52, no. 8, pp. 1934–1943, Aug. 2004.

[16] F. Kong, M. Zada, H. Yoo, and M. Ghovanloo, "Adaptive matching transmitter with dual-band antenna for intraoral tongue drive system," *IEEE Trans. Biomed. Circuits Syst.*, vol. 12, no. 6, pp. 1279–1288, Dec. 2018.

[17] T. Sano *et. al.*, "A 6.3mW BLE transceiver embedded RX image-rejection filter and TX harmonic-suppression filter reusing on-chip matching network," in *IEEE Int. Solid-State Circuits Conf. Dig. Tech. Papers*, Feb. 2015, pp. 240–241.

[18] J. Prummel *et al.*, "A 10 mW bluetooth low-energy transceiver with on-chip matching," *IEEE J. Solid-State Circuits*, vol. 50, no. 12, pp. 3077–3088, Dec. 2015.

[19] M. Song *et al.*, "An energy-efficient antenna impedance detection using electrical balance for single-step on-chip tunable matching in wearable/implantable applications," *IEEE Trans. Biomed. Circuits Syst.*, vol. 11, no. 6, pp. 1236–1244, Dec. 2017.

[20] S. Kousai *et. al.*, "Polar antenna impedance detection and tuning for efficiency improvement in a 3G/4G CMOS power amplifier," in *IEEE Int. Solid-State Circuits Conf. (ISSCC) Dig. Tech. Papers*, Feb. 2015, pp. 240–241.

[21] Y. Yoon, H. Kim, H. Kim, K.-S. Lee, C.-H. Lee, and J. S. Kenney, "A 2.4-GHz CMOS power amplifier with an integrated antenna impedance mismatch correction system," *IEEE J. Solid-State Circuits*, vol. 49, no. 3, pp. 608–621, Mar. 2014.

[22] B. Wiser, *et. al.*, "A 1.53 mm3 crystal-less standards-compliant bluetooth low energy module for volume constrained wireless sensors," in *Proc. Symp. VLSI Circuits*, Jun. 2019, pp. 84–85.

[23] Y. Shi *et. al.*, "A 10 mm3 syringe-implantable near-field radio system on glass substrate," in *Proc. IEEE Int. Solid-State Circuits Conf. Dig. Tech. Papers*, Feb. 2016, pp. 448–449.

[24] L.-X. Chuo *et. al.*, "A 915MHz asymmetric radio using Q-enhanced amplifier for a fully integrated 3 $\times$ 3 $\times$ 3 mm3 wireless sensor node with 20m non-line-of-sight communication," in *IEEE Int. Solid-State Circuits Conf. Dig. Tech. Papers*, Feb. 2017, pp. 132–133.

[25] F. Maksimovic, *et. al.*, "A crystal-free single-chip micro mote with integrated 802.15.4 compatible transceiver, sub-mW BLE compatible beacon transmitter, and cortex m0," in *Proc. Symp. VLSI Circuits*, Jun. 2019, pp. 88–89.

[26] A. Alghaihab *et. al.*, "A crystal-less BLE transmitter with -86dBm frequency-hopping back-channel WRX and over-the-air clock recovery from a GFSK-modulated BLE packet," in *IEEE Int. Solid-State Circuits Conf. Dig. Tech. Papers*, Feb. 2020, pp. 472–473.
[27] M. Tamura *et. al.*, "A 0.5 V BLE transceiver with a 1.9 mW RX achieving −96.4 dBm sensitivity and 4.1 dB adjacent channel rejection at 1 MHz offset in 22 nm FDSOI," in *IEEE Int. Solid-State Circuits Conf. (ISSCC) Dig. Tech. Papers*, Feb. 2020, pp. 468–469.
[28] T. van Nunen, E. Huismans, R. Mestrom, H. Visser, and M. Bentum, "Diy electromagnetic phantoms for biomedical wireless power transfer experiments," in *Proc. Wireless Power Week*, Jun. 2019, pp. 399–404.
[29] C. Bachmann *et al.*, "A 3.5 mW 315/400 MHz IEEE802.15.6/proprietary mode digitally-tunable radio SoC with integrated digital baseband and MAC processor in 40 nm CMOS," in *Proc. Symp. VLSI Circuits*, Jun. 2015, pp. 94–95.
[30] M.-C. Lee *et al.*, "A CMOS medradio transceiver with supply-modulated power saving technique for an implantable brain–machine interface system," *IEEE J. Solid-State Circuits*, vol. 54, no. 6, pp. 1541–1552, Dec. 2019.
[31] J. Bae, N. Cho, and H.-J. Yoo, "A 490uW fully MICS compatible FSK transceiver for implantable devices," in *Proc. Symp. VLSI Circuits*, Jun. 2009, pp. 36–37.
[32] B. Zhao, N. Kuo, B. Liu, Y. Li, L. Iotti, and A. M. Niknejad, "A batteryless padless crystalless 116 μm $\times$ 116 μm "Dielet" near-field radio with on-chip coil antenna," *IEEE J. Solid-State Circuits*, vol. 55, no. 2, pp. 249–260, Feb. 2020.

Minyoung Song (Member, IEEE) received the B.S. and Ph. D. degrees in electrical engineering from Korea University, Seoul, South Korea, in 2006 and 2013, respectively. He has been with the Interuniversity Microelectronics Centre (IMEC), The Netherlands, since 2016, where he is currently a Senior Researcher. He was a Senior Engineer with Samsung Electronics, Hwaseong, from 2013 to 2016. He was a Visiting Scholar with the University of California, Los Angeles, from 2008 to 2009 and with the University of California, Santa Cruz, 2012. His current research interests include energy-efficient digitally assisted RFIC, frequency synthesizers/clock generators, and high-speed wireline transceivers. Dr. Song was the recipient of the IEEE Seoul Section Student Paper Contest Bronze Award in 2007 and 2010, respectively.

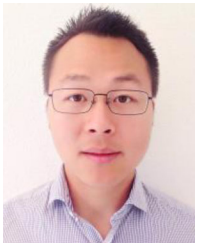

Ming Ding (Member, IEEE) received the B.Sc. degree from the Huazhong University of Science and Technology, China, in 2009, the M.Sc. degree (cum laude) from the Eindhoven University of Technology, The Netherlands, in 2011, and the Ph.D degree from the Eindhoven University of Technology, in 2019. From 2011, he has been with Interuniversity Microelectronics Centre (IMEC), The Netherlands, where he is currently a Senior Research Scientist. His research has resulted in about 30 technical publications and several patents. His research interests include ultra-low-power circuit design for IoT applications and implantable applications. His research has resulted in about 30 technical publications and several patents.

Evgenii Tiurin started his professional career as an Electronics Engineer in 1994. As such, he was with various R&D Centres and production companies in Russia, Sweden, South Korea, and The Netherlands, mostly focusing on digital and mixed-signal ASICs for wireless communication and networking applications. Starting from 2015, he has been working for Interuniversity Microelectronics Centre (IMEC)-Netherlands, Eindhoven, The Netherlands as Digital ASIC Design and Verification Engineer.

Kai Xu (Student Member, IEEE) received the B.Sc. degree (summa cum laude) from Shandong Normal University, China, in 2012, and the M.Sc. degree in electronics engineering from Peking University, China, in 2015. He received the Ph.D. from University College Dublin (UCD), Ireland. From 2018 to 2019, he was with IMEC-Holst Center, Eindhoven, The Netherlands, as an RFIC Research and Development Intern. From 2013 to 2014, he was with IMEC/INTEC_Design Group (now IDLab), Ghent University, Belgium, as an Exchange Student. In 2015, he was a Visiting Scholar with Harvard University, Cambridge. From 2017 to 2018, he was a Visiting Research Assistant with the University of Macau, Macau. He held an industry internship at Beijing BLX IC Design Corporation, in 2017. He currently holds a postdoctoral position at UCD and Equal1 Labs, Ireland. His current research interests include CMOS ultra-low-power (ULP) RF and mixed-signal integrated circuits and systems for wireless/wireline communications and quantum computing.

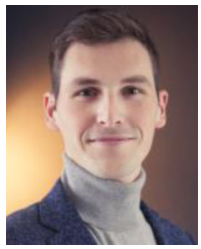

Erwin Allebes received the B.Sc. and M.Sc. degrees in electrical engineering from the Delft University of Technology, Delft, The Netherlands. Since 2019, he has been with Interuniversity Microelectronics Centre (IMEC), The Netherlands, where he is involved in ultralow-power radios and cellular IoT. His research interests include ultra-low-power circuit design for IoT applications such as low-power radios, digital PAs and frequency synthesizers/clock generators.

Gaurav Singh received the B.Tech degree from DAIICT, Gandhinagar, India, in 2007 and the M.Sc. (cum laude) degree in microelectronics from the Delft University of Technology, The Netherlands, in 2011. From 2007 to 2009, he was working with Cypress Semiconductor, India, as an Application Engineer defining next generation memory and mixed-signal programmable systems on chip products. From 2013 to 2019, he was with Qorvo, The Netherlands, where he worked on research and design of ultra-low-power radio SoCs for IoT applications. Since 2019, he has been working as a Senior Researcher with Interuniversity Microelectronics Centre (IMEC), The Netherlands, where he is leading the research and design of innovative ultra-low power RFICs and systems.

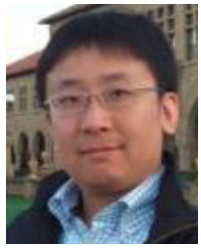

Peng Zhang received the B.S. and M.S. degrees in electrical engineering from the Huazhong University of Science and Technology, China, and Twente University, The Netherlands, in 2004 and 2007, respectively. In 2009, he received the Professional Doctorate degree in engineering and also in electrical engineering from the Eindhoven University of Technology, The Netherlands. Since 2010, he has been a Ph.D. Researcher with the Eindhoven University of Technology on reliable communication of ultra-low-power wireless design. Since 2014, he has been with Interuniversity Microelectronics Centre (IMEC), The Netherlands as a Researcher on architecture and algorithms design for wireless communication and radar systems. His research interests include wireless and radar signal processing and communication and information theory.

Hubregt J. Visser (Senior Member, IEEE) received the M.Sc. degree in electrical engineering from the Eindhoven University of Technology, Eindhoven, The Netherlands, in 1989, and the Ph.D. degree from the Eindhoven University of Technology and Katholieke Universiteit Leuven, Leuven, Belgium, in 2009. In 1990, after fulfilling his military service at TNO Physics and Electronics Laboratory, The Hague, The Netherlands, he joined the same laboratory as a civilian. He has participated in projects concerning near-field antenna measurements, monolithic microwave integrated circuits design, and phased-array antenna design. In 1996–1997, he was stationed at the European Space Research and Technology Centre, Noordwijk, The Netherlands, where he worked on array antenna modeling. In 2001, he joined TNO Science and Industry, Eindhoven, working on antenna miniaturization. In 2009, he joined imec, Eindhoven, The Netherlands, where he works on Wireless Power Transfer. Since 2014, he has been a Full Professor with the Eindhoven University of Technology, where he teaches antenna theory. He holds 12 patents, has written seven book chapters, and is author of the books *Array and Phased Array Antenna Basics* (Wiley, 2005), *Approximate Antenna Analysis for CAD* (Wiley, 2009), and *Antenna Theory and Applications* (Wiley, 2012). He was co-organizer and Co-Chair of the IEEE 2019 Wireless Power Week in London.

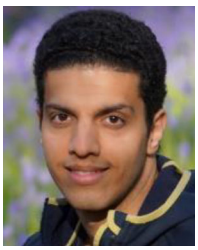

Reza Aminzadeh (Student Member, IEEE) received the M.Sc. degree from Sharif University of Technology, Iran, in 2014 and the Ph.D. degree from Ghent University, Belgium, in 2020, both in electrical engineering. In 2019, he was a Visiting Researcher at the Institute of Electronics and Telecommunications of Rennes (IETR), Rennes, France. Since 2020, he has been a Postdoctoral Researcher at Waves (UGent-imec). From 2012 to 2014, he was a Researcher at the Sharif University of Technology. He served as a technical program committee member for National Iranian Student Conference on Electrical Engineering (ISCEE) during 2011-2014. He is the author or coauthor of more than 30 peer-reviewed scientific journals and conference papers in bioelectromagnetics. His research interests include numerical and experimental dosimetry, wearable antenna design, on/in body radio wave propagation, measurement and theoretical modeling of biological tissues. dielectric properties, and development of tissue-equivalent phantoms for the mm-wave band, including the 5G technology. Dr. Aminzadeh is the recipient of the third Best Platform Presentation and Scientific Paper Award in BioEM2018.

Wout Joseph (Senior Member, IEEE) was born in Ostend, Belgium on October 21, 1977. He received the M. Sc. degree in electrical engineering from Ghent University, Ghent, Belgium, in July 2000. He received the Ph. D. degree in March 2005; this work dealt with measuring and modelling of electromagnetic fields around base stations for mobile communications related to the health effects of the exposure to electromagnetic radiation. He was a Postdoctoral Fellow of the FWO-V (Research Foundation – Flanders) from 2007 to 2012. Since October 2009, he has been a Professor in the domain of "Experimental Characterization of wireless communication systems." He has been a PI with Interuniversity Microelectronics Centre (IMEC) since 2017. His research interests are electromagnetic field exposure assessment, propagation for wireless communication systems, antennas and calibration. Furthermore, he specializes in wireless performance analysis and Quality of Experience.

Luc Martens (Member, IEEE) received the M.Sc. degree in electrical engineering from the Ghent University, Belgium, in July 1986. From September 1986 to December 1990, he was a Research Assistant with the Department of Information Technology (INTEC) of the same university. During this period, his scientific work was focused on the physical aspects of hyperthermia, a cancer therapy. He is author or co-author of more than 275 peer-reviewed journal publications and contributed to four books. His research work dealt with electromagnetic and thermal modelling and with the development of measurement systems for that application. This work led to the Ph.D. degree in December 1990. Since 1991, he has been managing the WAVES Research Group, INTEC. His research group is also associated with Interuniversity Microelectronics Centre (IMEC), where he is a Research Director. On 1st of April 1993, he was appointed as an Associate Professor with Ghent University and currently he is a Full Professor with the same university. His expertise and current research interests are in modelling and measurement of antennas and electromagnetic channels for wireless systems, of electromagnetic exposure e.g., around telecommunication networks and systems such as cellular base station antennas, in applications of electromagnetic fields to health, localization, and in AI and recommender systems.

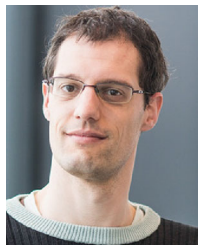

Nick Van Helleputte (Member, IEEE) received the M.S. degree in electrical engineering from the Katholieke Universiteit Leuven, Belgium, in 2004 and and the Ph.D. degree from the same institute in 2009 (MICAS Research Group). He was with Interuniversity Microelectronics Centre (IMEC) in 2009 and is currently an R&D Manager of the Connected Health Solutions group. His research interest is on ultra-low-power circuits for biomedical applications. Dr. Helleputte is an SSCS Member (SSCS Distinguished Lecturer 2017–2018) and served on the Technical Program Committee of VLSI Circuits Symposium and ISSCC.

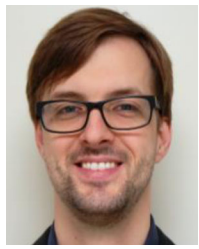

Christian Bachmann received the Ph.D. degree in electrical engineering from the Graz University of Technology, Graz, Austria, in a collaboration with Infineon Technologies in 2011. He was with Interuniversity Microelectronics Centre (IMEC) in 2011, working on ultra-low-power DSP and wireless communication systems, digital baseband (DBB) processing, and hardware/software co-design. He is currently a Program Manager of IMEC's Secure Proximity and Sensitive Networks programs, addressing R&D challenges for high-accuracy, secure wireless localization with Bluetooth as well as Ultra-Wideband (UWB) and for advanced ultra-low power (ULP) RF wireless transceiver circuits enabling next-gen automotive, medical, and IoT applications.

Yao-Hong Liu (Senior Member, IEEE) received the Ph.D. degree from National Taiwan University, Taiwan, in 2009. He was with Terax, Via Telecom (now Intel), and Mobile Devices, Taiwan, from 2002 to 2010, working on Bluetooth, WiFi and cellular wireless SoC products. Since 2010, he has been with Interuniversity Microelectronics Centre (IMEC), The Netherlands. His current position is the Principal Membership of Technical Staff, and he is leading the development of the ultra-low power wireless IC design. His research interest focuses on energy-efficient RF transceivers and radar for IoT and healthcare applications. He is currently a Technical Program Committee of IEEE, ISSCC, and RFIC symposium.